EES Solar

PAPER

View Article Online
View Journal

Cite this: DOI: 10.1039/d5el00164a

Tuning the surface nanoroughness of the recombination junction for high-performance perovskite–silicon tandem solar cells

Yifeng Zhao, †[a] Esma Ugur,†[bc] Arsalan Razzaq,[b] Thomas G. Allen,[b] Paul Procel Moya,[a] Adi Prasetio,[b] Imil F. Imran,[b] Cem Yilmaz,[c] Rik Hooijer,[c] Jian Huang,[c] Katarina Kovačević,[a] Yi Zheng,[a] Luana Mazzarella,[a] Erkan Aydin,*[c] Stefaan De Wolf *[b] and Olindo Isabella *[a]

The monolithic integration of perovskite top cells on textured crystalline silicon affords efficient tandem devices with strong prospects for large-scale applications. Such integration has primarily relied on state-of-the-art recombination junctions, which typically comprise transparent conductive oxides and molecular self-assembled monolayer (SAM) contacts. However, the potential influence of bottom cell nanoroughness, which may vary based on specific processing routes and technologies, has received far less attention. Here, we systematically engineered the top surface nanoroughness of silicon heterojunction solar cells to examine its impact on monolithic perovskite–silicon tandem solar cells. We employed two approaches: (i) varying the thickness of (*n*)-type hydrogenated nanocrystalline silicon ((*n*)nc-Si:H) layers or (ii) applying a plasma treatment using a hydrogen and carbon dioxide gas mixture before the deposition of (*n*)nc-Si:H layers. Both methods enhanced the conductivity and crystallinity of (*n*)nc-Si:H layers and increased the surface nanoroughness, with plasma treatment enabling the efficient realization of distinct nanoroughness in thin (*n*)nc-Si:H (15-nm-thick) layers. Our results reveal that the surface nanoroughness imposed by (*n*)nc-Si:H layers influences the SAM anchoring, leading to increased work function shifts and improved SAM/perovskite interface quality, thereby impacting the overall tandem device performance. Notably, tandem devices incorporating higher-nanoroughness bottom cells achieved increased fill factors, dominating the observed tandem efficiency enhancements, with a peak efficiency of 32.6% enabled by a 30-second-long plasma treatment.

Received 2nd October 2025
Accepted 7th January 2026

DOI: 10.1039/d5el00164a

rsc.li/EESSolar

Broader context

Perovskite–silicon tandem solar cells have surpassed the theoretical efficiency limits of single-junction devices. While most research efforts have optimized the perovskite top cell and its interfaces, the silicon bottom cell has remained relatively underexplored even though it plays a crucial role in the overall device performance. Our study finds that nanoscale surface roughness originating from the top layers of the bottom cell and transferred to the recombination junction significantly influences key processes such as self-assembled monolayer anchoring, perovskite crystallization, and interface quality. The deposition of hydrogenated nanocrystalline silicon layers and plasma treatments applied before their deposition altered the nanoscale surface roughness of textured silicon surfaces, yielding improved fill factors and higher device efficiencies. Our approach complements existing strategies focused on perovskite optimization and introduces a new design parameter for tandem solar cells. In addition, gained insights are broadly relevant to silicon heterojunction and other crystalline silicon technologies that employ similar thin-film layers. Our work on engineering the nanoscale surface morphology affords more efficient and scalable tandem architectures as well as supports the accelerated adoption of high-performance photovoltaics.

Introduction

Perovskite–silicon tandem solar cells offer the prospect of achieving high power conversion efficiencies (PCEs) beyond the theoretical single-junction limitations at an affordable cost. To realize this potential, efforts have largely focused on optimizing the perovskite top cells, including optoelectronic engineering of interfaces.[1–7] Particular attention has been given to the recombination junction, which typically involves transparent conductive oxides (TCO) and SAM charge-selective contacts,

[a]*Photovoltaic Materials and Devices, Delft University of Technology, 2628 CD, Delft, The Netherlands. E-mail: O.Isabella@tudelft.nl*

[b]*Center for Renewable Energy and Storage Technologies (CREST), Physical Sciences and Engineering Division (PSE), King Abdullah University of Science and Technology (KAUST), Thuwal 23955-6900, Saudi Arabia. E-mail: stefaan.dewolf@kaust.edu.sa*

[c]*Department of Chemistry, Ludwig-Maximilians-Universität München (LMU), 81377, Munich, Germany. E-mail: erkan.aydin@cup.uni-muenchen.de*

† Both authors have contributed equally.

onto which the perovskite layers are directly deposited.[8–10] On the other hand, achieving high-performance tandems also requires careful consideration of the silicon bottom cell.

In silicon heterojunction (SHJ) bottom cells used for solution-processed perovskite–silicon tandem devices, various (*n*)-type Si layers (acting as electron transport layers in the bottom cell and hereafter referred to as (*n*)-layers) have been implemented. The most commonly used are hydrogenated amorphous silicon ((*n*)a-Si:H),[11–22] nanocrystalline silicon ((*n*)nc-Si:H)[10,23–26] and oxygen-alloyed layers ((*n*)nc-SiO_x:H).[27–29] Among these, nc-Si:H-based layers exhibit more favorable optoelectronic properties,[30–45] enabling their widespread use in state-of-the-art industrial single-junction SHJ solar cells.[33,46,47] When properly optimized for tandem devices, nc-Si:H-based layers also enhance light coupling into the c-Si absorber by improving refractive index matching at the interfaces between the subcells.[48–50] Notably, nc-Si:H-based layers are mixed-phase materials composed of nanocrystals embedded within an amorphous matrix.[51,52] The top surfaces of crystal grains in nc-Si:H-based layers can adopt different morphologies, often dome-shaped, which give rise to surface nanoroughness.[53–57] Such surface morphologies of nc-Si:H-based layers can be explained by the cone-kinetics model,[58] where sparsely formed nanocrystal nuclei grow nearly isotropically (crystalline phase) and faster than the surrounding amorphous matrix (amorphous phase),[59] whose slower growth 'clips' the expanding nanocrystals into dome-shaped features. Because this morphology is governed by the growth-rate ratio between the two phases, variations in film thickness and deposition parameters (*e.g.*, doping, plasma frequency or alloy composition) can alter the resulting surface morphology.[60–66] Due to the substrate-dependent growth characteristics of nc-Si:H-based layers,[51] strategies that modify the substrate surface to enable prompt nucleation of nanocrystals[67–70] are also expected to affect the surface roughness of these layers. Even though surface morphology strongly affects the SAM anchoring and, in turn, solution-processed perovskite film quality,[10,71–73] the specific effect of nc-Si:H-induced bottom cell surface nanoroughness on overall tandem device performance has often been overlooked.

Here, we investigate how the surface nanoroughness of textured c-Si bottom cells, originating from variations in (*n*)nc-Si:H thin films, influences the performance of monolithic perovskite–silicon tandem solar cells. We tailored the (*n*)nc-Si:H nanoroughness by (i) adjusting the thickness of the (*n*)nc-Si:H layers and (ii) applying plasma treatment using a hydrogen (H_2) and carbon dioxide (CO_2) gas mixture for varying durations prior to (*n*)nc-Si:H layer depositions. We found that systematic variation of the plasma treatment duration allows for controlled variation of the surface nanoroughness of textured c-Si bottom cells, which promoted improved tin-doped indium oxide (ITO)/hole transport layer (HTL)/perovskite interfaces and ultimately enhanced the tandem device performance.

Results and discussion

We fabricated perovskite–silicon tandem solar cells using bottom cells based on two different thicknesses of (*n*)nc-Si:H layers: ~15 nm (Type-1) and 25 nm (Type-2) (Fig. 1A). Although the single junction performance for these bottom cells exhibited comparable open circuit voltage (V_{OC}) and fill factor (FF) values (Fig. S1), the tandem performance differed significantly (Fig. 1B). The V_{OC} of the two types of tandem devices varied by more than 30 mV, which is larger than the variations attributed to recombination layer TCO differences.[10] Also, the tandems based on the 15-nm-thick (*n*)nc-Si:H layer (Type-1) yielded FF values as low as $73.1 \pm 3.7\%$. To assess the role of underlying layer morphology in device homogeneity, we investigated long-range thin-film heterogeneities, such as pin holes as shown in Fig. S2, using photoluminescence (PL) imaging. Type-1 tandems exhibited several localized dark regions, indicative of shunt pathways (red circles in Fig. 1C). Considering that all perovskite sub-cell processing parameters were identical, these features cannot be attributed to variations in the perovskite deposition itself. We therefore performed cross-sectional scanning electron microscopy (SEM) analysis to examine the perovskite absorber and (*n*)nc-Si:H/TCO in the same images. The analysis revealed apparent (*n*)nc-Si:H morphology differences between Type-1 and Type-2 devices. In particular, tandems incorporating the 25-nm-thick (*n*)nc-Si:H layer (Type-2) exhibited a more clearly defined silicon nanocrystalline domain structure.[10,53–56]

Tuning the surface nanoroughness of (*n*)nc-Si:H layers

We first investigated the formation of surface nanoroughness by depositing (*n*)nc-Si:H layers with thicknesses ranging from ~15 nm to 70 nm on textured c-Si wafers coated with (*i*)a-Si:H layers. This approach aimed at achieving SHJ device-relevant growth of (*n*)nc-Si:H layers, considering their substrate-dependent growth characteristics.[51] As the thickness of (*n*)nc-Si:H increases, the nanoroughness on textured c-Si wafers also increases (Fig. S3). We attribute this to increased crystallinity of the deposited films, as evidenced by a gradual decrease in activation energy (E_a), increments of dark conductivity (σ_d), and enhanced crystalline phase signals in the Raman spectra (Fig. S4).[60–63] However, thicker (*n*)nc-Si:H layers require longer deposition times and lead to increased infrared absorption, resulting in higher parasitic losses in the bottom cell and consequently reduced short-circuit current density (J_{SC}) values in perovskite–silicon tandem devices (Fig. S5 and S6). To mitigate this, we alternatively employed a plasma treatment using a mixture of H_2 and CO_2 gases prior to the (*n*)nc-Si:H deposition. This method, reported to generate pre-formed nanocrystal seeds that facilitate subsequent crystal growth,[74] is expected to be particularly effective in minimizing the amorphous incubation phase through the rapid nucleation of nanocrystals. The possible mechanisms responsible for the generation of pre-formed nanocrystal seeds may be associated with the mixed CO_2 and H_2 plasma, which generates increased strained bonds[75–77] and promotes hydrogen-driven reorganization in a-Si:H,[60,78–81] thereby enabling the formation of nanocrystal seeds. Furthermore, hydrogen-dominated CO_2 and H_2 plasma conditions[74] can induce H_2 plasma-driven chemical transport[82,83] and CO_2 plasma-induced oxidation of the reactor walls,[83] collectively creating plasma environments having higher effective H_2 to SiH_4 dilution that favor the pre-formation of nanocrystal seeds.

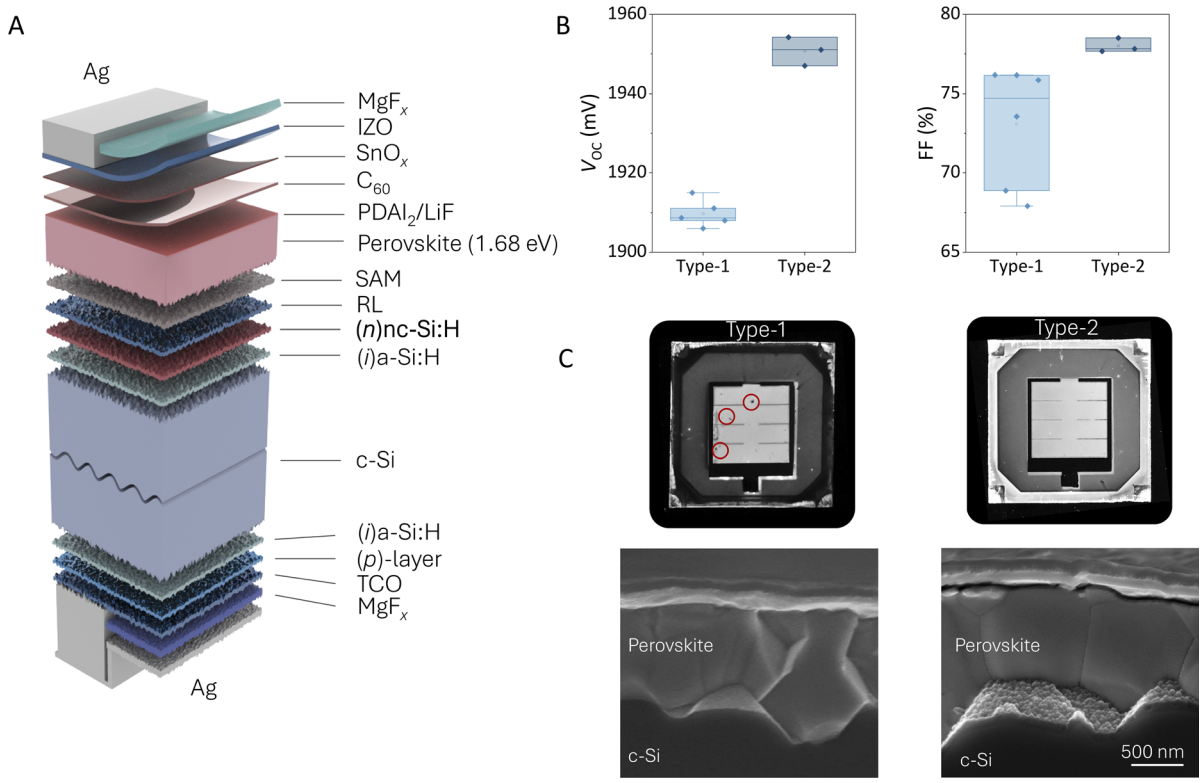

Fig. 1 (A) The schematic of the monolithic perovskite–silicon tandem device, (B) the V_{OC} and FF of the fabricated tandem devices featuring different bottom cells, with Type-1 and Type-2 based on 15-nm-thick and 25-nm-thick (*n*)nc-Si:H layers, respectively, and (C) the PL images and cross-sectional SEM micrographs of respective devices. Note that Type-1 features 10-nm-thick ITO and Type-2 has 5-nm-thick IZO as the interconnecting recombination layer (RL) and rear TCO layer.

For the plasma treatment process, (*n*)nc-Si:H layer thickness was fixed at 15 nm while the plasma treatment duration was systematically varied (Fig. 2). Increasing the plasma treatment duration led to progressively enhanced surface nanoroughness (Fig. 2A). Even a 15-second-long plasma treatment exhibits the first signs of nanoroughness formation, characterized by densely distributed nanoscale protrusions emerging on the pyramid surfaces. Extending the plasma treatment duration to 60 seconds led to the formation of aggregated crystalline grains, evidenced by the appearance of larger, spherical surface features.[53–56] For comparison, the surface morphology of the sample with a 6-nm-thick (*n*)a-Si:H layer, as shown in Fig. S7, displays relatively negligible surface nanoroughness. To further assess nanoroughness on textured substrates, we performed Atomic Force Microscopy (AFM) measurements on c-Si with various (*n*)-layers (Fig. S8). The overall morphological changes observed by AFM are consistent with those identified in SEM micrographs. However, quantitative roughness analysis and high-fidelity nanoscale interpretation were hindered by the pronounced pyramidal texture of the c-Si wafers, cantilever-facet angle limitations, and associated measurement artefacts. Although not explicitly investigated in this study, it is worth noting that different nc-Si:H-based layers, such as (*n*)nc-SiO_x:H layers and (*p*)nc-Si:H-based layer stacks,[84,85] can exhibit distinct morphological, electrical, and structural properties depending on their thickness and the plasma treatment duration, highlighting the necessity to understand material-specific behavior for device integration (Fig. S9–S11).

We then examined the electrical and microstructural properties of the (*n*)nc-Si:H layers. Unlike the gradual improvements of electrical properties observed with increasing (*n*)nc-Si:H layer thickness (Fig. S4), 40-nm-thick layers treated with just 15 seconds of plasma treatment showed a sharp decrease in E_a from 336 meV to 41 meV and notable increments of σ_d from 3.6×10^{-4} S cm^{-1} to 4.8 S cm^{-1}, as well as improved crystallinity (Fig. 2B and C). Notably, the 15-nm-thick layers also exhibited a conductivity boost from 3.6×10^{-5} S cm^{-1} to 0.6 S cm^{-1} upon 15 seconds of plasma treatment applied before (*n*)nc-Si:H deposition, comparable to that of a 100-nm-thick (*n*)nc-Si:H layer (Fig. S4).[74]

We assessed the effect of plasma treatments on charge transport by measuring the contact resistivity (ρ_c) of (*n*)-type contact stacks (Fig. 2D and E). Unlike the ρ_c that showed little variation and remained around 90 mΩ cm^2 when changing (*n*) nc-Si:H thicknesses (Fig. S13), plasma treatments durations up to 30 seconds reduced the ρ_c from around 88 mΩ cm^2 to 79 mΩ cm^2, while a 60-second-long treatment caused an increase of ρ_c to around 89 mΩ cm^2, likely due to the formation of thicker interfacial oxide layers (Fig. S14).[40] On the other hand, we found that plasma treatments degraded the passivation quality of the samples, potentially due to dehydrogenation of the underlying (*i*)a-Si:H layers (Fig. 2F).[74] As discussed previously, exposure to a CO_2 plasma introduces oxygen and alters the local bonding

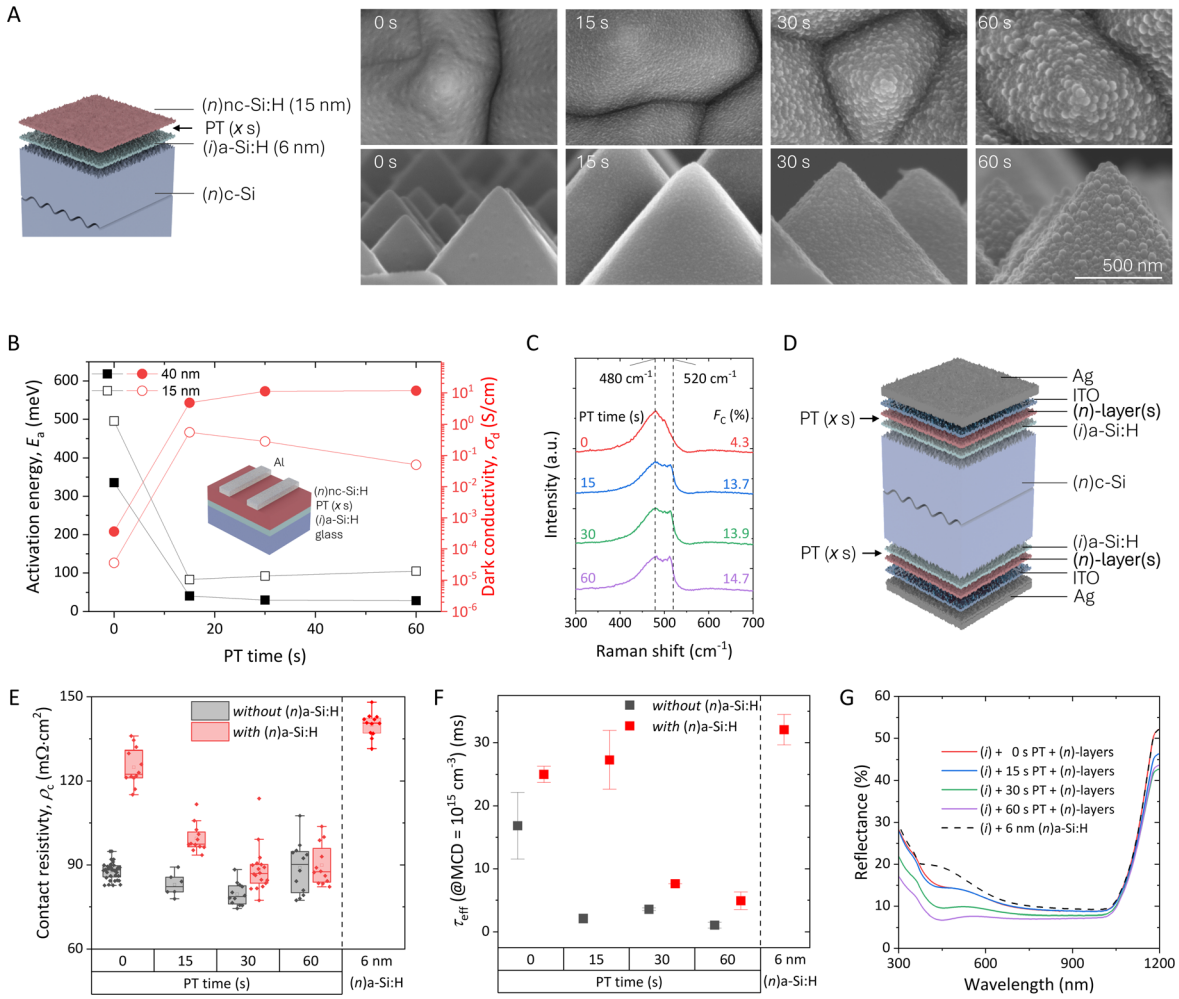

Fig. 2 (A) The SEM micrographs of textured c-Si samples with 15-nm-thick (*n*)nc-Si:H layers having plasma treatments (PTs) of different durations applied prior to (*n*)nc-Si:H layer depositions as shown in schematics of the stacks on the left (top and bottom rows displaying top and cross-sectional view images, respectively). (B) The activation energy (E_a) and dark conductivity (σ_d) of (*n*)nc-Si:H layers with thicknesses of 40 and 15 nm and (C) the Raman spectra and crystalline fraction (F_C) of 40-nm-thick (*n*)nc-Si:H layers having plasma treatments of different durations applied prior to (*n*)nc-Si:H layer depositions, deposited on 10-nm-thick (*i*)a-Si:H-coated glass substrates. Raman spectra of 15-nm-thick (*n*)nc-Si:H layers are shown in Fig. S12. Although films deposited on flat glass substrates differ from those on textured c-Si wafers, they adequately approximate material properties relevant to device integration. Note, as the green laser ($\lambda_{laser} = 514$ nm) has a penetration depth of a few hundred nanometers in the studied (*n*)nc-Si:H layers, their crystalline fraction is underestimated due to non-negligible signals from the 10-nm-thick (*i*)a-Si:H layer underneath. (D) The schematic of the symmetrical *n*–*n* device stack used for contact resistivity (ρ_c) and lifetime (measured prior to metallization) measurements. (E) The extracted ρ_c of (*n*)-type contact stack (including a space-charge layer inside the (*n*)c-Si bulk, (*i*)a-Si:H, (*n*)-layers (stacks), ITO and Ag) and (F) the effective minority carrier lifetime (τ_{eff}) values for samples featuring 15-nm-thick (*n*)nc-Si:H layers, without or with a 2-nm-thick (*n*)a-Si:H capping layer, as a function of plasma treatment duration. The ρ_c and τ_{eff} of samples featuring the 6-nm-thick (*n*)a-Si:H layers are added in (E) and (F) for comparisons. (G) The reflectance spectra of (*i*)a-Si:H-coated (6-nm-thick) textured samples featuring 15-nm-thick (*n*)nc-Si:H + 2-nm-thick (*n*)a-Si:H layers ((*n*)-layers) with varied durations of plasma treatments. The reflectance spectrum of the sample with a 6-nm-thick (*n*)a-Si:H layer is added in (G) as a reference.

environment within the a-Si:H layer, promoting bond breaking and structural rearrangement. Such treatment has been shown to increase structural disorder and may generate a significant amount of non-bonded hydrogen within the amorphous network, eventually leading to dehydrogenation.[74,75] Besides, CO_2 plasma was also reported to form interface dipoles that impede electron collection.[86] An optimized hydrogen plasma treatment improves (*i*)a-Si:H passivation by driving hydrogen to the c-Si/(*i*)a-Si:H interface to saturate dangling bonds and by creating a hydrogen-rich layer with increased formation of monohydrides and some polyhydrides at internal surfaces associated with larger voids that serve as reservoirs for further defect passivation.[87–90] In the mixed CO_2 and H_2 plasma treatment, these competing mechanisms coexist, and despite improved field-effect passivation, introduced by the overlaying more conductive (*n*)nc-Si:H (see Fig. 2B),[31] the CO_2-induced degradation remains dominant (Fig. 2F). To mitigate this, we introduced a 2-nm-thick (*n*)a-Si:H capping layer on top of the (*n*)nc-Si:H layer. The introduction of the (*n*)a-Si:H layer may supply additional hydrogen at the c-Si/(*i*)a-Si:H interface, passivating

dangling bonds and improving the interface quality (Fig. S15). Further experiments quantifying the hydrogen content in the (*i*)a-Si:H layer and at the c-Si/(*i*)a-Si:H interface are needed to verify this hypothesis. As seen from Fig. 2F, this additional (*n*)a-Si:H layer improved the effective carrier lifetime (τ_{eff}) across all samples without altering the surface morphology induced by the underlying (*n*)nc-Si:H layer (Fig. S16). Furthermore, the capping layer reduced the passivation deterioration caused by the sputtering-induced damage during ITO deposition.[85] It is well known that passivation degradation at the c-Si/a-Si:H interface can occur during TCO sputtering due to ion bombardment damage[91] or plasma luminescence.[92,93] An (*n*)a-Si:H layer, which more effectively mitigates ion penetration (for example, oxygen ions[85,94]) and absorbs more high-energy photons, can therefore better preserve passivation quality after TCO sputtering compared with (*n*)nc-Si:H layers. However, the additional (*n*)a-Si:H slightly increased the ρ_c, presumably due to its lower σ_d and higher E_a (>200 meV) than (*n*)nc-Si:H layers.[85,95] Still, this slight increase of ρ_c is considered acceptable for efficient charge carrier transport, given the reduced light intensity reaching the bottom cell in tandem devices and the one-dimensional current flow through the contact in the tandem cell.[96,97] Overall, samples with (*n*)nc-Si:H layers having plasma treatments prior to their depositions, with and without the (*n*)a-Si:H capping layer, show statistically lower ρ_c as compared to the (*n*)a-Si:H-only counterparts. Moreover, as shown in Fig. 2G, a longer plasma treatment duration resulted in a gradual reduction in reflectance, particularly at shorter wavelengths, compared to the case of 6-nm-thick (*n*)a-Si:H, evidencing the formation of enhanced surface nanoroughness of (*n*)nc-Si:H layers.[98] A similar trend was observed after depositing a 10-nm-thick ITO layer (Fig. S17), confirming the persistence of this optical behavior. Despite the higher nanoroughness of samples with thicker (*n*)nc-Si:H layers, no significant reduction in reflection was observed (Fig. S18). Furthermore, depositing a 10-nm-thick ITO layer on top of the (*n*)nc-Si:H layer resulted in a more apparent surface nanoroughness across all samples, even though the overall surface morphology is still governed by the underlying (*n*)nc-Si:H layers (see Fig. 2A and S17 for the plasma treatment duration series and Fig. S3 for the (*n*)nc-Si:H thickness series). It is worth noting that TCO properties, such as surface morphology, mobility, carrier concentration, and work function can be affected by the underlying Si layers and the choice of TCO layers.[63,73] These TCO properties collectively influence the effectiveness of the recombination junction, in conjunction with the adjacent layers. While in this study, SEM analysis shows no discernible morphological differences between 10-nm-thick ITO layers deposited on (*n*)a-Si:H and (*n*)nc-Si:H layers (see Fig. S7B and S16B). Moreover, no difference in work function is observed for ITO layers deposited on (*n*)a-Si:H and (*n*)nc-Si:H layers (discussed in the following section). Therefore, we expect only a limited influence of the (*n*)-layers on 10-nm-thick ITO properties under our processing conditions, although further studies are required to gain deeper insights into this aspect. Due to the pronounced passivation loss and the increased ρ_c observed with a 60-second plasma treatment, such a condition was excluded from subsequent tandem cell experiments.

Impact on SAM deposition and perovskite film formation

We first analyzed surface energy by measuring a solution contact angle of HTL-SAM on textured c-Si wafers coated with ITO layers and different (*n*)-layers, since SAM anchoring changes the wettability of the surface. The sample with a 6-nm-thick (*n*)a-Si:H layer exhibited the lowest contact angle (~70°), while the 15-nm-thick (*n*)nc-Si:H sample showed a higher value of ~85° (Fig. 3A). Applying plasma treatments prior to the (*n*)nc-Si:H deposition further increased the contact angle to more than 100°, lowering the surface energy. Thicker (*n*)nc-Si:H layers also exhibited increased contact angles (Fig. S19). Next, we investigated the impact of the same parameters on the work function shift (ΔWF) for (*n*)nc-Si:H/ITO/SAM stacks. We included SAMs in this analysis as they induce charge dipoles at the TCO interface, resulting in a ΔWF that enhances the charge selectivity.[10] Kelvin probe measurements on (*n*)nc-Si:H/ITO stacks with various (*n*)-layers revealed similar WF values (~4.61–4.62 eV) (Fig. 3B). After SAM deposition as used in our device fabrication, we found systematic WF shifts towards higher values, with larger ΔWF observed for those with higher contact angle values and greater surface nanoroughness (Fig. 3C).[73] Given that ΔWF scales with the dipole surface density,[99] this suggests that the molecular packing of SAMs is influenced by the underlying surface nanoroughness.[10]

As surface tension force can influence the perovskite grain formation, we examined (*n*)nc-Si:H conditions, modulated by plasma treatment duration, on the overlying perovskite morphology (Fig. 3D).[100] Cross-sectional SEM images show that all samples exhibited complete perovskite coverage, while the film with the 30-second-long plasma treatment displayed slightly larger and more uniformly distributed grains. GIWAXS measurements show that among the different plasma treatment durations, the 30-second-long plasma treatment condition produced the most pronounced preferential 45° orientation of the (100) reflection relative to the surface of the substrate (Fig. 3D), which is known to improve carrier mobilities and photovoltaic performance.[101,102] To gain further insights into the optoelectronic quality of perovskite films, we carried out absolute PL imaging. Perovskites deposited on textured silicon with extended plasma treatment duration exhibited higher PL intensity compared to 6-nm-thick (*n*)a-Si:H and 15-nm-thick (*n*)nc-Si:H (Fig. S22) and a more uniform quasi-Fermi level splitting (QFLS, $\Delta\mu$), with a value of 1290 meV for the 30-second plasma treatment (Fig. 3E), indicating reduced non-radiative recombination. By controlling plasma treatment duration, the surface properties of (*n*)-layers can be tuned to simultaneously enhance perovskite film formation and its electronic interfacial quality on textured silicon substrates.

Performance of perovskite–silicon tandem solar cells

The *J*–*V* characteristics of tandem devices are presented in Fig. 4. Compared to devices with a 6-nm-thick (*n*)a-Si:H layer, which exhibited relatively lower V_{OC} (~1920 mV) and FF (~68%), the one endowed with 15-nm-thick (*n*)nc-Si:H layer effectively mitigates the shunting behavior in devices using the (*n*)a-Si:H layer, resulting in V_{OC} and FF values of ~1945 mV and

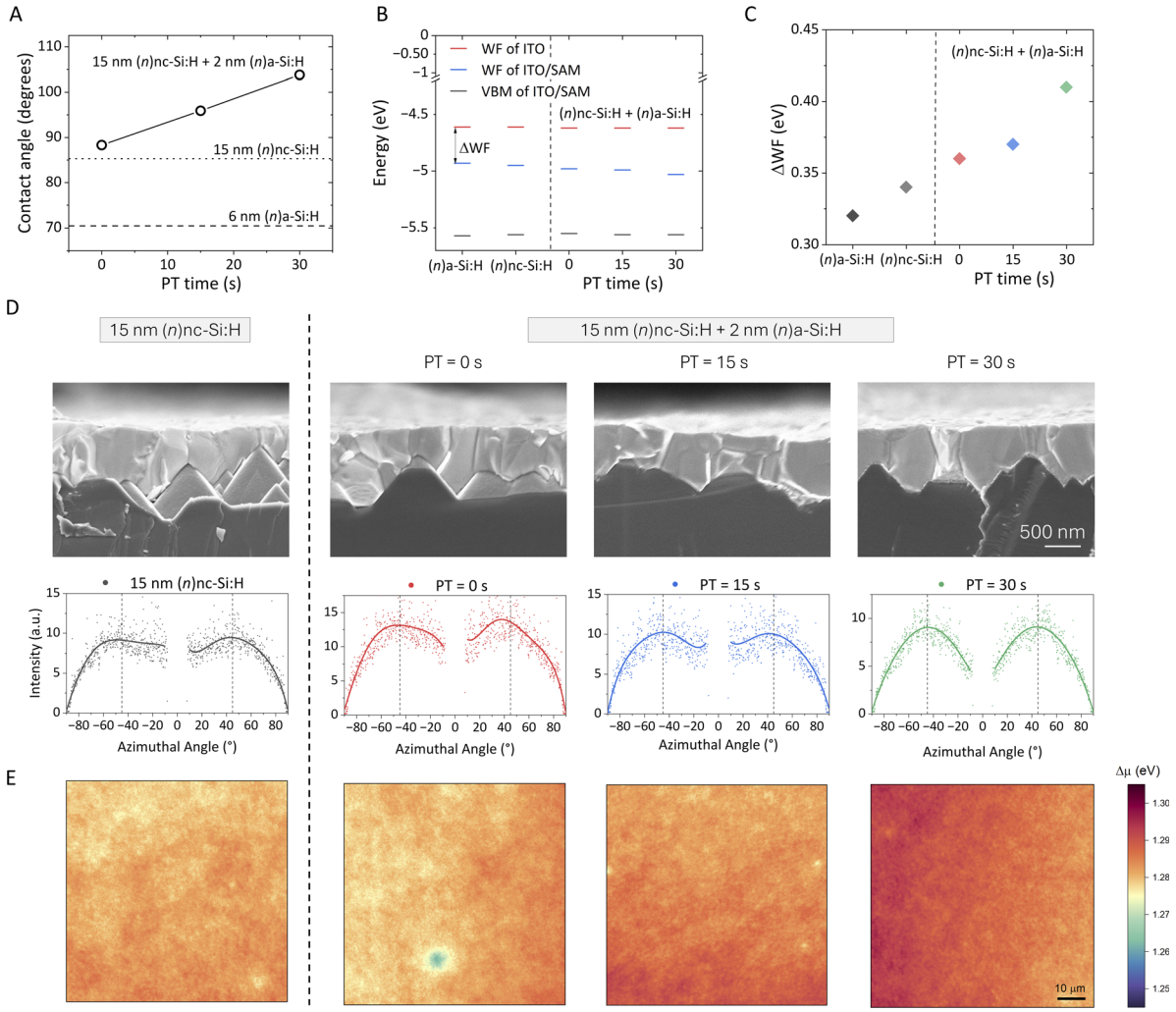

Fig. 3 (A) Contact angle values after HTL-SAM deposition on textured c-Si wafers featuring various plasma treatment (PT) durations on (*n*)nc-Si:H layers with 10-nm-thick ITO. The dashed lines in the plot represent the contact angles of samples with 6-nm-thick (*n*)a-Si:H and 15-nm-thick (*n*)nc-Si:H layers. (B) Valence band maximum (VBM) and WF values, and (C) ΔWF of (*n*)-layer/ITO/SAM (stack) with various plasma treatment durations before and after SAM deposition. (D) Cross-sectional SEM micrographs and azimuthally integrated intensity of the (100) reflection from GIWAXS measurements (Fig. S20). (E) QFLS ($\Delta\mu$) images of perovskite films deposited on different (*n*)-layer/ITO/SAM stacks without and with plasma treatment. The SEM micrograph of the sample featuring the (*n*)a-Si:H layer is shown in Fig. S21.

~75%, respectively (Fig. 4A). These differences are primarily attributed to the higher WF shift after SAM deposition (Fig. 3C) associated with increased nanoroughness when implementing a 15-nm-thick (*n*)nc-Si:H layer. Besides, the lower ρ_c of 15-nm-thick (*n*)nc-Si:H-based contact stacks as compared to 6-nm-thick (*n*)a-Si:H-based contact stacks (Fig. 2E) may also contribute to higher FF values in tandem devices featuring the (*n*)nc-Si:H layer. Adding a 2-nm-thick (*n*)a-Si:H capping layer on the 15-nm-thick (*n*)nc-Si:H layer slightly improves V_{OC} of tandem solar cells, likely due to enhanced passivation quality of such (*n*)-layer (Fig. 2F and S23B).[85] For tandem devices having a 15-second-long plasma treatment, although their bottom cell precursors exhibited slightly higher median iV_{OC} (Fig. S23B) and better SAM/perovskite interface and perovskite film quality (Fig. 3) compared to the ones without plasma treatment, the resulting tandem devices showed only a marginal increase in median V_{OC}, remaining largely comparable overall between these two conditions. Furthermore, a 30-second-long plasma treatment resulted in reduced bottom cell precursors' iV_{OC} by approximately 15 to 20 mV relative to samples with 15-second-long plasma treatment. However, this difference is expected to be less pronounced in tandem devices due to reduced illumination for bottom cells. Besides, this loss in bottom cell can be further partially compensated by the improved SAM/perovskite interface quality and perovskite film quality (Fig. 3). Consequently, the final tandem devices having a 30-second-long plasma treatment exhibited improved FF, and only a slightly reduced median V_{OC} that is not significantly different from the other samples. As expected, J_{SC} values remain comparable across all samples (Fig. 4B and C). Finally, we achieved efficiencies up to 32.6% by applying a plasma treatment duration of 30 seconds for 15-nm-thick (*n*)nc-Si:H with 2-nm-thick (*n*)a-Si:H layers.

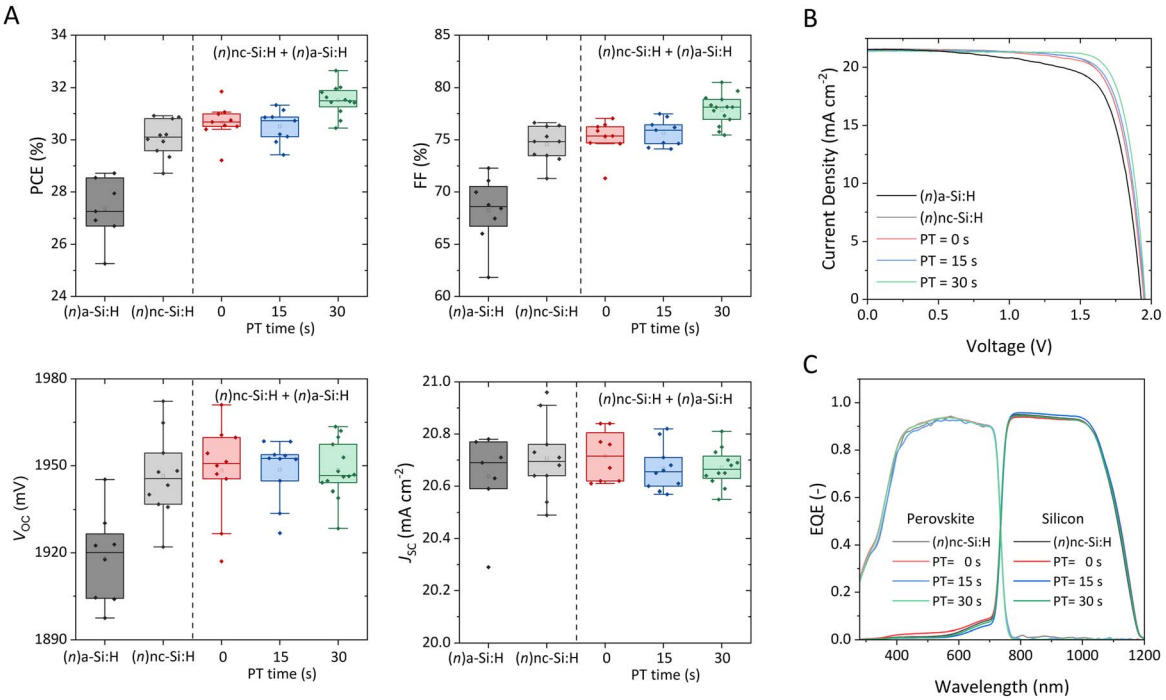

Fig. 4 (A) The J–V parameters of perovskite–silicon tandem solar cells with varying (n)-layers (stacks), namely, 6-nm-thick (n)a-Si:H layer, 15-nm-thick (n)nc-Si:H layer without plasma treatment (labeled as (n)nc-Si:H), and 15-nm-thick (n)nc-Si:H + 2-nm-thick (n)a-Si:H layer stack with varied durations of plasma treatment. (B) The J–V characteristics of the best devices for each (n)-layer (stack), and (C) EQE spectra of respective tandem solar cells. The EQE spectrum of the tandem device with the (n)a-Si:H layer is shown in Fig. S24.

Conclusions

In this work, we have presented a new perspective for advancing high-efficiency perovskite–silicon tandem solar cells by demonstrating the critical role of bottom cell surface nanoroughness in device performance. In silicon bottom cells, nanoroughness can be tuned either by varying the thickness of (n)nc-Si:H layers or by applying a plasma treatment utilizing a hydrogen and carbon dioxide gas mixture for different durations prior to their depositions. These approaches modify not only the optoelectronic and microstructural properties of the (n)-layers but also the surface morphology of textured c-Si bottom cells. Increased nanoroughness leads to higher contact angles and larger ΔWF after SAM deposition, which results in improved HTL/perovskite interface quality. Our approach *via* optimizing plasma treatment enables efficient control of surface morphology, allowing thin (n)nc-Si:H layers to achieve high surface nanoroughness, reducing process time and enhancing tandem cell performance compared to their thicker counterparts without plasma treatment. Our results highlight c-Si bottom cell surface morphology control as a powerful yet underexplored strategy for further improving perovskite–silicon tandem solar cells and accelerating their industrialization, with broader implications for various nc-Si:H-based layers already employed in industrial SHJ solar cell production and other c-Si solar cell technologies.

Experimental details

Fabrication of c-Si bottom cells and contact resistivity samples

4-inch, (n)-type float-zone (FZ) silicon wafers with a thickness of 260–280 μm were utilized for bottom cell fabrication. A double-sided random pyramid texture with submicron features (averaging below 1 μm in height) was formed through wet chemical etching in a 0.5% KOH solution at 77 °C, employing a TS41 additive. Subsequently, the wafers underwent a standard RCA cleaning protocol at 75 °C, first in an RCA1 solution ($NH_4OH : H_2O_2 : H_2O = 1 : 1 : 6$) to remove organic contaminants and then in an RCA2 solution ($HCl : H_2O_2 : H_2O = 1 : 1 : 6$) to eliminate metallic impurities. Following a hydrofluoric acid (HF) (0.55%) dipping, wafers were loaded into a multi-chamber radio-frequency (RF, 13.56 MHz) or very-high-frequency (VHF, 40.68 MHz) plasma-enhanced chemical vapor deposition (PECVD) cluster tool (Elettrorava S.p.A.). PECVD depositions started with the (i)a-Si:H/(n)-layer (stack).[85,90] After a brief vacuum break, the wafers were flipped for subsequent deposition of the (i)a-Si:H/(p)nc-SiO_x:H/(p)nc-Si:H layer stack.[84,90] By default, an optimized hydrogen plasma treatment (HPT) was applied after the deposition of (i)a-Si:H layers,[85] optionally followed by a plasma treatment (PT) using a hydrogen and carbon dioxide gas mixture. Subsequently, 10-nm-thick tin-doped indium oxide (ITO) layers were symmetrically deposited *via* an RF magnetron sputtering (Polyteknic AS) tool at room temperature. The wafers were then annealed in air at 180 °C for 5 minutes. A geometrical factor of 1.7 was applied to adjust the deposition time for

textured surfaces relative to flat substrates. Local rear contacts were formed using screen-printed Ag grid lines with a width of ~60 μm and a spacing of ~0.9 mm. These contacts were sintered by annealing the wafers at 200 °C for 15 minutes in a box furnace. Afterwards, a 200 nm MgF_2 film was thermally evaporated to form a rear reflector. The rear contact was then finalized with a 120 nm layer of sputtered Ag, followed by an annealing step at 200 °C for 10 minutes in ambient air to recover any sputtering-induced damage. Finally, the wafers were laser-cut into 2.2 × 2.2 cm^2 square pieces for integration into tandem solar cell structures.

For contact resistivity measurements, symmetrical Si thin-films and TCO layers, as previously described, were deposited, followed by annealing in air at 180 °C for 5 minutes. The samples were then completed with 500 nm of thermally evaporated Ag on both sides (Provac PRO500S).

Fabrication of perovskite top-cells for tandem devices

The Si bottom cells were subjected to UV-ozone treatment for 700 seconds and were modified by 2PACz (TCI) with a solution using 1 mg mL^{-1} concentration in ethanol and spin coating at 5000 rpm for 30 seconds, followed by post-annealing at 100 °C for 10 minutes in a N_2 filled glove box. 1.7 M $Cs_{0.05}FA_{0.8}$-$MA_{0.15}Pb(I_{0.745}Br_{0.255})_3$ perovskite precursor solution, which delivers 1.68 eV optical band gap, was prepared by mixing FAI, MABr, CsI, PbI_2, and $PbBr_2$ in a solvent of DMF:DMSO with a volume ratio of 4 : 1. The perovskite films were spin-coated at 2000 rpm for 45 seconds, and then the spinning was accelerated to 7000 rpm for the last 8 seconds. 200 μL chlorobenzene was dropped onto the substrates at the start of this acceleration. After the rotation ceased, the substrates were transferred onto a hotplate of 100 °C and were annealed for 20 minutes. Following perovskite deposition, 1,3-propane diammonium iodide ($PDAI_2$) surface treatment was applied to regulate the surface potential at the perovskite/C_{60} interface using a previously reported recipe.[103] To displace contact between the C_{60} and perovskite layers, we employed ~1 nm of evaporated LiF. As an electron transport layer (ETL), 12-nm-thick C_{60} was evaporated, and then 10-nm-thick SnO_2 was deposited by Picosun atomic layer deposition (ALD) tool by following the same recipe as in our previous studies.[10] Front IZO contacts were sputtered from a 3-inch IZO ceramic target on top of the SnO_2 through a shadow mask. The thickness of the front IZO was 40 nm. An Ag finger with a thickness of 500 nm was thermally evaporated using a high-precision shadow mask with a deposition rate of 2 Å s^{-1}. Concluding the tandem devices, 100 nm MgF_2 was thermally evaporated as an anti-reflection layer with a deposition rate of 1 Å s^{-1} (Plasmaterials, 99.9%). To ensure the precise thicknesses of C_{60}, IZO, and LiF, spectroscopic ellipsometry was used for calibration. The evaporation rate and thickness of each experiment were monitored using quartz crystal microbalance sensors. All thermal evaporation processes were performed on an Angstrom EvoVac thermal evaporation system. All chemicals were used without further purification.

Tandem solar cell performance analysis

In-house current–voltage (*I–V*) measurements were conducted using a Wavelabs Sinus 220 LED-based solar simulator. For spectrum calibration, a Fraunhofer ISE-certified calibration cell was used, and no spectral mismatch factor was applied in the process. The area of illumination for the devices was precisely 1.04 cm^2, determined using a laser-cut shadow mask coated with black paint. The device measurements were carried out at a scan speed of 150 mV s^{-1}. The external quantum efficiency (EQE) measurements were conducted using PV-Tools LOANA equipment. When measuring perovskite top cells, the tandem devices were light-biased using IR LEDs (930 nm). In the case of measuring silicon bottom cells, the tandem devices were light-biased using a blue LED (440 nm) to saturate the subcells. All device characterization experiments were conducted under ambient air conditions with a relative humidity (RH) of approximately 50–60%.

Absolute PL imaging

To exclude the influence of environmental factors such as humidity and oxygen, we encapsulated the samples in a nitrogen glove box. The PL spectra of the samples were collected using a hyperspectral imaging system coupled to a microscope with 2 nm spectral resolution (Photon *etc.* IMA). Samples were excited using a 405 nm laser at ~1 sun illumination condition (before the measurement, the power density of the laser was adjusted with a reference perovskite solar cell) to calculate the quasi-Fermi level splitting (QFLS, $\Delta\mu$). A home-built MatLab code using the relation reported earlier was employed to calculate the $\Delta\mu$.[104]

PESA

Photoelectron spectroscopy in air (PESA) measurements were performed using a Riken AC-2 setup equipped with a UV light source. The valence band maximum (VBM) was determined by linear fitting of ground and photoemission signals from the samples that were prepared for device fabrication.

Kelvin probe

For Kelvin probe measurements, a standard gold tip with a diameter of 2 mm was used within an inert-atmosphere glovebox at room temperature. The WF of the tip was first calibrated against a clean gold reference ($WF_{tip} = 5.1\ eV - CPD_{Au}$). The sample WF was then determined using $WF_{sample} = WF_{tip} + CPD_{sample}$, ensuring values are referenced to the absolute vacuum level. Measurements used an SPS040 instrument with a 50 mV amplitude, 90 Hz frequency, 13.5 kHz scan rate, 30 averages per point, and a gain of 4.

Kelvin Probe Force Microscopy (KPFM)

A Multimode AFM from Digital Instruments (Veeco Metrology Group), fitted with a Bruker scanning head, was used to conduct topographic imaging and surface potential measurements in ambient air at room temperature. The measurements were carried out using an SCM-PIT V2 AFM tip, based on an RFESP-75

AFM probe coated with a platinum–iridium (PtIr) reflective layer. The tip was composed of antimony-doped silicon with a resistivity between 0.01 and 0.025 Ω cm. It had a rectangular shape with a nominal resonant frequency of 75 kHz and a spring constant of 4 N m^{-1}. Amplitude-modulated KPFM was employed, where the surface topography was first recorded in tapping mode during the initial scan, followed by surface potential mapping in a second pass.

Grazing-incidence wide-angle X-ray scattering (GIWAXS)

GIWAXS measurements were carried out on an Anton-Paar Saxspoint 2.0 system with a Primux 100 microfocus source with Cu-$K_{\alpha 1}$ radiation ($\lambda = 1.5406$ Å) and a Dectris Eiger R 1M 2D detector. Measurements were taken at a sample–detector distance of 121 mm.

Scanning electron microscopy (SEM)

A Hitachi Regulus 8230 was used for SEM analysis of textured c-Si samples with silicon thin-films and ITO layers. Images were acquired at 5 kV. The morphology of perovskite films on textured Si was analyzed using an in-house FEI Helios Nanolab G3 UC DualBeam SEM. Images were acquired at 2 kV, to minimize beam-induced damage to the perovskite film while ensuring adequate resolution and contrast, using a TLD detector. Samples, prepared from the active area, were mounted on silver paste, and no additional conductive coating was applied.

Characterization of bottom cells and contact resistivity samples

Spectroscopic ellipsometry (SE) (M-2000DI system, J.A. Woollam Co., Inc.) was employed for extracting the optical constants and the thickness of thin-film layers deposited on glass substrates (Corning Eagle XG). Temperature-dependent dark current–voltage (I–V) measurements with temperature sweep from 130 °C to 60 °C were conducted to determine the dark conductivity (σ_d) and activation energy (E_a). For these measurements, samples featuring 300-nm-thick Al strips were evaporated onto doped layers on glass substrates. A Raman spectrometer (Renishaw inVia Micro-Raman microscope) equipped with a green laser ($\lambda_{laser} = 514$ nm) was deployed for obtaining the Raman spectra of doped Si thin-film layers. A photoconductance lifetime tester (Sinton WCT-120) was used to monitor the passivation quality of samples during their fabrication. Additionally, the resistivity of symmetric samples was obtained *via* dark I–V measurements using Kelvin probe contacts and a Keithley 2601B source measure unit. The method as described in a previous study was used for extracting the contact resistivity (ρ_c).[84] A PerkinElmer Lambda 1050 system was used to measure the wavelength-dependent reflectance (R) of the testing samples, and to reflect device-relevant conditions, samples with 10-nm-thick ITO layers were annealed at 180 °C for 5 minutes in an air atmosphere.

Atomic Force Microscopy (AFM)

A HORIBA OmegaScope AFM operated in tapping mode, equipped with a NANOSENSORS PPP-NCHR cantilever featuring a guaranteed AFM tip radius of curvature <10 nm, was used for assessing the nanoroughness of the textured c-Si samples featuring different (n)-layers (stacks) studied in this work.

Conflicts of interest

The authors declare no competing interests.

Data availability

The data supporting the findings of this study are available within the article and its supplementary information (SI). Additional datasets generated and analyzed during the current study are available from the corresponding authors on reasonable request. Supplementary information. See DOI: https://doi.org/10.1039/d5el00164a.

Acknowledgements

This study was partially funded by the Nord Storm project that has received funding from the CET Partnership No. CETP-2022-00360/NWO EP.1602.22.003 and by the European Research Council (ERC) under the European Union's Horizon Europe Research and Innovation Program (INPERSPACE, Grant Agreement No. 101077006). The KAUST team was supported by the KAUST Office of Sponsored Research (OSR) under award number ORFS-CRG11-2022-5035. Jian Huang thanks the China Scholarship Council (CSC) for funding his PhD scholarship (grant number 202 306 010 063). Yifeng Zhao thanks Youri Blom and Yingwen Zhao for their assistance with Raman spectra analysis, and Riccardo Brondolin for help with AFM measurement.

References

1 Y. Wang, Y. Wang, F. Gao and D. Yang, Efficient Monolithic Perovskite/Silicon Tandem Photovoltaics, *Energy Environ. Mater.*, 2024, **7**, e12639.
2 Z. Ying, X. Yang, X. Wang and J. Ye, Towards the 10-Year Milestone of Monolithic Perovskite/Silicon Tandem Solar Cells, *Adv. Mater.*, 2024, **36**, 2311501.
3 F. Hou, *et al.*, Monolithic perovskite/silicon tandem solar cells: a review of the present status and solutions toward commercial application, *Nano Energy*, 2024, 109476.
4 E. Aydin, *et al.*, Pathways toward commercial perovskite/silicon tandem photovoltaics, *Science*, 2024, **383**, eadh3849.
5 F. Fu, *et al.*, Monolithic perovskite-silicon tandem solar cells: from the lab to fab?, *Adv. Mater.*, 2022, **34**, 2106540.
6 X. Li, *et al.*, How to enable highly efficient and large-area fabrication on specific textures for monolithic perovskite/silicon tandem solar cells?, *Information Functional Materials*, 2024, **1**, 160–180.

7 O. Er-raji, *et al.*, Electron accumulation across the perovskite layer enhances tandem solar cells with textured silicon, *Science*, 2025, eadx1745.
8 J. Liu, *et al.*, Efficient and stable perovskite-silicon tandem solar cells through contact displacement by MgF_x, *Science*, 2022, **377**, 302–306.
9 X. Y. Chin, *et al.*, Interface passivation for 31.25%-efficient perovskite/silicon tandem solar cells, *Science*, 2023, **381**, 59–63.
10 E. Aydin, *et al.*, Enhanced optoelectronic coupling for perovskite/silicon tandem solar cells, *Nature*, 2023, **623**, 732–738.
11 Y. Hou, *et al.*, Efficient tandem solar cells with solution-processed perovskite on textured crystalline silicon, *Science*, 2020, **367**, 1135–1140.
12 F. H. Isikgor, *et al.*, Concurrent cationic and anionic perovskite defect passivation enables 27.4% perovskite/silicon tandems with suppression of halide segregation, *Joule*, 2021, **5**, 1566–1586.
13 S. Zhumagali, *et al.*, Linked nickel oxide/perovskite interface passivation for high-performance textured monolithic tandem solar cells, *Adv. Energy Mater.*, 2021, **11**, 2101662.
14 J. Liu, *et al.*, 28.2%-efficient, outdoor-stable perovskite/silicon tandem solar cell, *Joule*, 2021, **5**, 3169–3186.
15 X. Zheng, *et al.*, Photoactivated p-doping of organic interlayer enables efficient perovskite/silicon tandem solar cells, *ACS Energy Lett.*, 2022, **7**, 1987–1993.
16 J. Liu, *et al.*, Efficient and stable perovskite-silicon tandem solar cells through contact displacement by MgF_x, *Science*, 2022, **377**, 302–306.
17 N. Ren, *et al.*, 50 °C low-temperature ALD SnO_2 driven by H_2O_2 for efficient perovskite and perovskite/silicon tandem solar cells, *Appl. Phys. Lett.*, 2022, **121**, 033502.
18 E. Ugur, *et al.*, Front-contact passivation through 2D/3D perovskite heterojunctions enables efficient bifacial perovskite/silicon tandem solar cells, *Matter*, 2023, **6**, 2919–2934.
19 Z. Liu, *et al.*, Reducing perovskite/C60 interface losses via sequential interface engineering for efficient perovskite/silicon tandem solar cell, *Adv. Mater.*, 2024, **36**, 2308370.
20 L. Liu, *et al.*, Hydrophobic Hydrogen-Bonded Polymer Network for Efficient and Stable Perovskite/Si Tandem Solar Cells, *Angew. Chem., Int. Ed.*, 2024, **63**, e202317972.
21 Y. Ding, *et al.*, Multifunctional Spacer in 2D/3D Wide-Bandgap Perovskite for Monolithic Perovskite/Silicon Tandem Solar Cells, *Sol. RRL*, 2024, **8**, 2400189.
22 X. Ji, *et al.*, Multifunctional Buffer Layer Engineering for Efficient and Stable Wide-Bandgap Perovskite and Perovskite/Silicon Tandem Solar Cells, *Angew. Chem.*, 2024, **136**, e202407766.
23 A. A. Said, *et al.*, Sublimed C60 for efficient and repeatable perovskite-based solar cells, *Nat. Commun.*, 2024, **15**, 708.
24 C. Wang, *et al.*, Solvent-Assisted Surface Modification Using Metallocene-Based Molecules for High-Efficiency Perovskite/Silicon Tandem Solar Cells, *Adv. Energy Mater.*, 2024, **14**, 2401039.
25 M. De Bastiani, *et al.*, Monolithic perovskite/silicon tandems with >28% efficiency: role of silicon-surface texture on perovskite properties, *Adv. Funct. Mater.*, 2023, **33**, 2205557.
26 M. De Bastiani, *et al.*, Efficient bifacial monolithic perovskite/silicon tandem solar cells *via* bandgap engineering, *Nat. Energy*, 2021, **6**, 167–175.
27 P. Tockhorn, *et al.*, Nano-optical designs for high-efficiency monolithic perovskite–silicon tandem solar cells, *Nat. Nanotechnol.*, 2022, **17**, 1214–1221.
28 A. Harter, *et al.*, Double-sided nano-textured surfaces for industry compatible high-performance silicon heterojunction and perovskite/silicon tandem solar cells, *Prog. Photovoltaics*, 2023, **31**, 813–823.
29 J. Liu, *et al.*, Perovskite/silicon tandem solar cells with bilayer interface passivation, *Nature*, 2024, **635**, 596–603.
30 P. Procel-Moya, Y. Zhao and O. Isabella, Unlocking the potential of carrier-selective contacts: key insights for designing c-Si solar cells with efficiency beyond 28%, *Sol. Energy Mater. Sol. Cells*, 2025, **285**, 113504.
31 P. Procel, G. Yang, O. Isabella and M. Zeman, Theoretical evaluation of contact stack for high efficiency IBC-SHJ solar cells, *Sol. Energy Mater. Sol. Cells*, 2018, **186**, 66–77.
32 Y. Zhao, *et al.*, Strategies for realizing high-efficiency silicon heterojunction solar cells, *Sol. Energy Mater. Sol. Cells*, 2023, **258**, 112413.
33 H. Lin, *et al.*, Silicon heterojunction solar cells with up to 26.81% efficiency achieved by electrically optimized nanocrystalline-silicon hole contact layers, *Nat. Energy*, 2023, **8**, 789–799.
34 L. V. Mercaldo, *et al.*, Potentials of mixed-phase doped layers in p-type Si heterojunction solar cells with ZnO: Al, *Sol. Energy Mater. Sol. Cells*, 2017, **169**, 113–121.
35 L. Mazzarella, *et al.*, p-type microcrystalline silicon oxide emitter for silicon heterojunction solar cells allowing current densities above 40 mA cm^{-2}, *Appl. Phys. Lett.*, 2015, **106**, 023902.
36 A. Lambertz, *et al.*, Microcrystalline silicon–oxygen alloys for application in silicon solar cells and modules, *Sol. Energy Mater. Sol. Cells*, 2013, **119**, 134–143.
37 K. Nakada, S. Miyajima and M. Konagai, Application of n-type microcrystalline silicon oxide as back reflector of crystalline silicon heterojunction solar cells, *Jpn J. Appl. Phys.*, 2015, **54**, 82301.
38 A. Richter, *et al.*, Versatility of doped nanocrystalline silicon oxide for applications in silicon thin-film and heterojunction solar cells, *Sol. Energy Mater. Sol. Cells*, 2018, **174**, 196–201.
39 D. Qiu, *et al.*, Front contact optimization for rear-junction SHJ solar cells with ultra-thin n-type nanocrystalline silicon oxide, *Sol. Energy Mater. Sol. Cells*, 2020, **209**, 110471.
40 K. Ding, U. Aeberhard, F. Finger and U. Rau, Silicon heterojunction solar cell with amorphous silicon oxide buffer and microcrystalline silicon oxide contact layers, *Phys. Status Solidi RRL*, 2012, **6**, 193–195.

41 S. Kirner, *et al.*, Silicon Heterojunction Solar Cells with Nanocrystalline Silicon Oxide Emitter: Insights into Charge Carrier Transport, *IEEE J. Photovolt.*, 2015, **5**, 1601–1605.
42 J. Haschke, *et al.*, Nanocrystalline silicon oxide stacks for silicon heterojunction solar cells for hot climates, *AIP Conf. Proc.*, 2018, **1999**, 30001.
43 L. Antognini, *et al.*, Influence of the Dopant Gas Precursor in P-Type Nanocrystalline Silicon Layers on the Performance of Front Junction Heterojunction Solar Cells, *IEEE J. Photovolt.*, 2021, **11**, 944–956.
44 Y. Xu, *et al.*, Heterojunction solar cells with n-type nanocrystalline silicon emitters on p-type c-Si wafers, *J. Non-Cryst. Solids*, 2006, **352**, 1972–1975.
45 J. Sritharathikhun, H. Yamamoto, S. Miyajima, A. Yamada and M. Konagai, Optimization of amorphous silicon oxide buffer layer for high-efficiency p-type hydrogenated microcrystalline silicon oxide/n-type crystalline silicon heterojunction solar cells, *Jpn J. Appl. Phys.*, 2008, **47**, 8452.
46 C. Yu, *et al.*, Industrial-scale deposition of nanocrystalline silicon oxide for 26.4%-efficient silicon heterojunction solar cells with copper electrodes, *Nat. Energy*, 2023, **8**, 1375–1385.
47 W. Wang, The progress of HJT in China, in *The 7th International Workshop on Silicon Heterojunction Solar Cells*, Catania, Italy, 2024.
48 L. Mazzarella, *et al.*, Infrared light management using a nanocrystalline silicon oxide interlayer in monolithic perovskite/silicon heterojunction tandem solar cells with efficiency above 25, *Adv. Energy Mater.*, 2019, **9**, 1803241.
49 Y. Zhao, *et al.*, Optical simulation-aided design and engineering of monolithic perovskite/silicon tandem solar cells, *ACS Appl. Energy Mater.*, 2023, **6**, 5217–5229.
50 Y. Zhao, *et al.*, *Optical Simulation-Aided Design and Optimization of SHJ Bottom Subcells for High-Efficiency Monolithic Perovskite/c-Si Tandem Solar Cells, SiliconPV2023, Oral Presentation, Session 6*, 2023.
51 P. Roca i Cabarrocas, N. Layadi, T. Heitz, B. Drévillon and I. Solomon, Substrate selectivity in the formation of microcrystalline silicon: Mechanisms and technological consequences, *Appl. Phys. Lett.*, 1995, **66**, 3609–3611.
52 P. Roca i Cabarrocas, New approaches for the production of nano-, micro-, and polycrystalline silicon thin films, *Phys. Status Solidi C*, 2004, **1**, 1115–1130.
53 B. Rezek, J. Stuchlık, A. Fejfar and J. Kočka, Local characterization of electronic transport in microcrystalline silicon thin films with submicron resolution, *Appl. Phys. Lett.*, 1999, **74**, 1475–1477.
54 V. S. Waman, *et al.*, Hydrogenated Nanocrystalline Silicon Thin Films Prepared by Hot-Wire Method with Varied Process Pressure, *J. Nanotechnol.*, 2011, **2011**, 242398.
55 L. Guo, J. Ding, J. Yang, G. Cheng and Z. Ling, Effects of high hydrogen dilution ratio on surface topography and mechanical properties of hydrogenated nanocrystalline silicon thin films, *Thin Solid Films*, 2011, **519**, 6039–6043.
56 M. Ledinský, *et al.*, Characterization of mixed phase silicon by Raman spectroscopy, *J. Non-Cryst. Solids*, 2006, **352**, 1209–1212.
57 P. Cuony, *et al.*, Mixed-phase p-type silicon oxide containing silicon nanocrystals and its role in thin-film silicon solar cells, *Appl. Phys. Lett.*, 2010, **97**, 213502.
58 C. W. Teplin, C.-S. Jiang, P. Stradins and H. M. Branz, Cone kinetics model for two-phase film silicon deposition, *Appl. Phys. Lett.*, 2008, **92**, 093114.
59 S. Guha and J. Yang, *High-Efficiency Amorphous Silicon and Nanocrystalline Silicon-Based Solar Cells and Modules: Final Technical Progress Report*, 30 January 2006-29 January 2008, 2008.
60 N. Layadi, P. Roca i Cabarrocas, B. Drévillon and I. Solomon, Real-time spectroscopic ellipsometry study of the growth of amorphous and microcrystalline silicon thin films prepared by alternating silicon deposition and hydrogen plasma treatment, *Phys. Rev. B:Condens. Matter Mater. Phys.*, 1995, **52**, 5136.
61 R. W. Collins, *et al.*, Evolution of microstructure and phase in amorphous, protocrystalline, and microcrystalline silicon studied by real time spectroscopic ellipsometry, *Sol. Energy Mater. Sol. Cells*, 2003, **78**, 143–180.
62 H. Fujiwara, M. Kondo and A. Matsuda, *Real-time Spectroscopic Ellipsometry Studies of the Nucleation and Grain Growth Processes in Microcrystalline Silicon Thin Films*, 2001, vol. 63, pp. 1–9.
63 A. Cruz, *et al.*, Influence of silicon layers on the growth of ITO and AZO in silicon heterojunction solar cells, *IEEE J. Photovolt.*, 2019, **10**, 703–709.
64 S. B. Amor, *et al.*, Effect of substrate temperature on microstructure and optical properties of hydrogenated nanocrystalline Si thin films grown by plasma enhanced chemical vapor deposition, *Sol. Energy*, 2014, **108**, 126–134.
65 M. Kondo, T. Ohe, K. Saito, T. Nishimiya and A. Matsuda, Morphological study of kinetic roughening on amorphous and microcrystalline silicon surface, *J. Non-Cryst. Solids*, 1998, **227**, 890–895.
66 T. Toyama, W. Yoshida, Y. Sobajima and H. Okamoto, Influence of boron doping on roughness microcrystalline silicon, *J. Non-Cryst. Solids*, 2008, **354**, 2204–2207.
67 Y. Park and S. Rhee, Effect of hydrogen plasma precleaning on the removal of interfacial amorphous layer in the chemical vapor deposition of microcrystalline silicon films on silicon oxide surface, *Appl. Phys. Lett.*, 1996, **68**, 2219–2221.
68 N. Pellaton Vaucher, *et al.*, Controlled nucleation of thin microcrystalline layers for the recombination junction in a-Si stacked cells, *Sol. Energy Mater. Sol. Cells*, 1997, **49**, 27–33.
69 J. P. Seif, *et al.*, Strategies for Doped Nanocrystalline Silicon Integration in Silicon Heterojunction Solar Cells, *IEEE J. Photovolt.*, 2016, **6**, 1132–1140.
70 G. Nogay, *et al.*, Nanocrystalline Silicon Carrier Collectors for Silicon Heterojunction Solar Cells and Impact on Low-Temperature Device Characteristics, *IEEE J. Photovolt.*, 2016, **6**, 1654–1662.
71 M. Chockalingam, N. Darwish, G. Le Saux and J. J. Gooding, Importance of the indium tin oxide substrate on the quality

of self-assembled monolayers formed from organophosphonic acids, *Langmuir*, 2011, **27**, 2545–2552.
72 R. Guo, *et al.*, Refining the substrate surface morphology for achieving efficient inverted perovskite solar cells, *Adv. Energy Mater.*, 2023, **13**, 2302280.
73 A. Harter, *Novel Wafer Topographies and Inter-contact Materials to Enable Industry-Compatible Monolithic Perovskite/silicon Heterojunction Tandem Solar Cells*, Technischen Universität Berlin, Berlin, 2025.
74 Y. Li, *et al.*, Flexible silicon solar cells with high power-to-weight ratios, *Nature*, 2024, **626**, 105–110.
75 L. Yan, *et al.*, Bifunctional CO_2 plasma treatment at the i/p interface enhancing the performance of planar silicon heterojunction solar cells, *Phys. Status Solidi RRL*, 2021, **15**, 2100010.
76 J. Huang, *et al.*, CO_2/H_2 treatment of p-type nanocrystalline silicon/intrinsic amorphous silicon interfaces on mass production line for efficiency improvement of silicon heterojunction solar cells, *Sol. Energy Mater. Sol. Cells*, 2026, **296**, 114070.
77 L. Wen, *et al.*, CO_2 Plasma Treatment To Prepare the Rear Emitter with a Boron-Doped Hydrogenated Amorphous/Nanocrystalline Silicon Stack for a High-Efficiency Silicon Heterojunction Solar Cell, *ACS Appl. Mater. Interfaces*, 2025, **17**, 8715–8726.
78 H. Fujiwara, M. Kondo and A. Matsuda, Microcrystalline silicon nucleation sites in the sub-surface of hydrogenated amorphous silicon, *Surf. Sci.*, 2002, **497**, 333–340.
79 H. Fujiwara, M. Kondo and A. Matsuda, Stress-induced nucleation of microcrystalline silicon from amorphous phase, *Jpn J. Appl. Phys.*, 2002, **41**, 2821.
80 K. Nakamura, K. Yoshino, S. Takeoka and I. Shimizu, Roles of atomic hydrogen in chemical annealing, *Jpn J. Appl. Phys.*, 1995, **34**, 442–449.
81 S. Sriraman, S. Agarwal, E. S. Aydil and D. Maroudas, Mechanism of hydrogen-induced crystallization of amorphous silicon, *Nature*, 2002, **418**, 62–65.
82 K. Saitoh, *et al.*, Role of the hydrogen plasma treatment in layer-by-layer deposition of microcrystalline silicon, *Appl. Phys. Lett.*, 1997, **71**, 3403–3405.
83 L. Yokomizo Newman, *et al.*, Why does CO2 plasma chamber seasoning favor nanocrystalline silicon growth?, *Appl. Phys. Lett.*, 2025, **127**, 233902.
84 Y. Zhao, *et al.*, Design and optimization of hole collectors based on nc-SiOx: H for high-efficiency silicon heterojunction solar cells, *Sol. Energy Mater. Sol. Cells*, 2021, **219**, 110779.
85 Y. Zhao, *et al.*, Ultra-thin electron collectors based on nc-Si: H for high-efficiency silicon heterojunction solar cells, *Prog. Photovoltaics*, 2022, **30**, 809–822.
86 S. Huang, *et al.*, Dipoles and defects caused by CO_2 plasma improve carrier transport of silicon solar cells, *Prog. Photovoltaics*, 2024, **32**, 283–290.
87 M. Mews, T. F. Schulze, N. Mingirulli and L. Korte, Hydrogen plasma treatments for passivation of amorphous-crystalline silicon-heterojunctions on surfaces promoting epitaxy, *Appl. Phys. Lett.*, 2013, **102**, 122106.
88 Y. Zhao, *et al.*, Doped hydrogenated nanocrystalline silicon oxide layers for high-efficiency c-Si heterojunction solar cells, *Prog. Photovoltaics*, 2020, **28**, 425–435.
89 M. Z. Burrows, U. K. Das, R. L. Opila, S. De Wolf and R. W. Birkmire, Role of hydrogen bonding environment in a-Si:H films for c-Si surface passivation, *J. Vac. Sci. Technol., A*, 2008, **26**, 683–687.
90 Y. Zhao, *et al.*, Effects of (*i*)a-Si: H deposition temperature on high-efficiency silicon heterojunction solar cells, *Prog. Photovoltaics*, 2022, **31**, 1170–1180.
91 A. Illiberi, P. Kudlacek, A. H. M. Smets, M. Creatore and M. C. M. Van De. Sanden, Effect of ion bombardment on the a-Si:H based surface passivation of c-Si surfaces, *Appl. Phys. Lett.*, 2011, **98**, 242115.
92 F. Lebreton, S. N. Abolmasov, F. Silva and P. Roca i Cabarrocas, *In situ* photoluminescence study of plasma-induced damage at the a-Si: H/c-Si interface, *Appl. Phys. Lett.*, 2016, **108**, 051603.
93 B. Demaurex, S. De Wolf, A. Descoeudres, Z. Charles Holman and C. Ballif, Damage at hydrogenated amorphous/crystalline silicon interfaces by indium tin oxide overlayer sputtering, *Appl. Phys. Lett.*, 2012, **101**, 171604.
94 S. Sheng, *et al.*, XPS depth profiling study of n/TCO interfaces for p-i-n amorphous silicon solar cells, *Appl. Surf. Sci.*, 2006, **253**, 1677–1682.
95 P. Procel, *et al.*, The role of heterointerfaces and subgap energy states on transport mechanisms in silicon heterojunction solar cells, *Prog. Photovoltaics*, 2020, **28**, 935–945.
96 L.-L. Senaud, *et al.*, Advanced method for electrical characterization of carrier-selective passivating contacts using transfer-length-method measurements under variable illumination, *J. Appl. Phys.*, 2021, **129**, 195707.
97 L.-L. Senaud, *et al.*, Transfer-Length Method Measurements Under Variable Illumination to Investigate Hole-Selective Passivating Contacts on c-Si (p) and c-Si (n) Wafers, *IEEE J. Photovolt.*, 2023, **13**, 422–431.
98 Z. Ying, *et al.*, Hierarchical Micro/Nanostructured Perovskite/Silicon Tandem Solar Cells with Fully Textured Solution-Processed Conformal Perovskite Absorbers, *ACS Energy Lett.*, 2024, **9**, 4018–4023.
99 I. Lange, *et al.*, Tuning the work function of polar zinc oxide surfaces using modified phosphonic acid self-assembled monolayers, *Adv. Funct. Mater.*, 2014, **24**, 7014–7024.
100 C. Bi, *et al.*, Non-wetting surface-driven high-aspect-ratio crystalline grain growth for efficient hybrid perovskite solar cells, *Nat. Commun.*, 2015, **6**, 7747.
101 C. Ma, *et al.*, Photovoltaically top-performing perovskite crystal facets, *Joule*, 2022, **6**, 2626–2643.
102 G. Zheng, *et al.*, Manipulation of facet orientation in hybrid perovskite polycrystalline films by cation cascade, *Nat. Commun.*, 2018, **9**, 2793.
103 H. Chen, *et al.*, Regulating surface potential maximizes voltage in all-perovskite tandems, *Nature*, 2023, **613**, 676–681.
104 E. Ugur, *et al.*, Enhanced cation interaction in perovskites for efficient tandem solar cells with silicon, *Science*, 2024, **385**, 533–538.

